



## Supplementary Materials for Spatiotemporal imaging of 2D polariton wave packet dynamics using free electrons

Yaniv Kurman<sup>†</sup>, Raphael Dahan<sup>†</sup>, Hanan Herzig Sheinfux, Kangpeng Wang, Michael Yannai, Yuval Adiv, Ori Reinhardt, Luiz H. G. Tizei, Steffi Y. Woo, Jiahao Li, James H. Edgar, Mathieu Kociak, Frank H. L. Koppens\*, Ido Kaminer\*

<sup>†</sup>These authors contributed equally to this work.

\*Corresponding author. Email: kaminer@technion.ac.il (I.K.); frank.koppens@icfo.eu (F.H.L.K.)

Published 11 June 2021, *Science* **372**, 1181 (2021)

DOI: 10.1126/science.abg9015

### This PDF file includes:

Materials and Methods  
Supplementary Text  
Figs. S1 to S7  
Table S1  
Captions for Movies S1 to S4  
References

### Other Supporting Online Material for this manuscript includes the following:

(available at [science.sciencemag.org/content/372/6547/1181/suppl/DC1](https://science.sciencemag.org/content/372/6547/1181/suppl/DC1))

Movies S1 to S4 (.mp4)

## Materials and Methods

### Experimental setup

The measurements were performed in an ultrafast transmission electron microscope (UTEM) based on a JEOL JEM-2100 Plus TEM with a LaB<sub>6</sub> electron gun and acceleration voltage of 40 kV–200 kV. We measured the electron–PhP interactions for both 80 kV and 200 kV. All the results presented in this paper are for 200 kV electrons due to the shorter electron pulse duration which increases the time resolution, and due to the larger electron energy that generates more counts per electron.

The UTEM operates as a pump–probe setup driven by a 40 Watt, 1,030-nm, ~270-fs laser (Carbide, Light Conversion) operating at a 1 MHz repetition rate and split into two pulses using a beam splitter. One pulse is converted into ultraviolet (UV) using two stages of second-harmonic generation and eventually excites the photo-electron probe. The second pulse is converted into variable wavelengths in the IR range through a difference frequency generation (DFG) process in an optical parametric amplifier (OPA, Light Conversion Orpheus). The temporal profile of the laser pulse is characterized through an independent PINEM measurement on a metallic film, see Fig. S3 (following an experiment similar to (45)). An additional spectral measurement was acquired through a Michelson interferometer near the DFG. Noticeably, the pump pulse experiences some distortion during its ~5-meter propagation until reaching the electron microscope column, creating part of the chirp (46). The delay  $\tau_d$  between the electron probe and the IR pump is controlled by a motorized stage. The TM-polarized IR pump has a spot size with standard deviation of ~30  $\mu\text{m}$ , a power of between 80 to 100 mW (fluence of  $\sim 2 \frac{\text{mJ}}{(\text{cm})^2}$ ) which is too weak to create significant heating in the sample, especially due to the PhP increased heat conductivity (47). This laser beam arrives in a side illumination, perpendicular to the direction of motion of the electron ( $z$ ). To prevent shadowing of the laser by the TEM grid and holder, our sample was tilted at an angle of 20°. This tilt also allowed us to control the coupling of the laser pulse into the PhP wavepacket.

The samples in our experiments are isotopically pure h<sup>11</sup>BN crystal flakes grown at atmospheric pressure (48) (exfoliated on a 20 nm thick Si<sub>3</sub>N<sub>4</sub> membrane, see sample preparation below). We determine the sample thickness using the EELS log ratio technique without the laser pump or a tilt (49), with the hBN inelastic mean free path taken from (50) and the Si<sub>3</sub>N<sub>4</sub> mean free path as the measured background.

The electron zero-loss peak (ZLP) is 0.9 eV prior to the interaction. After the interaction of the free electrons with the excited sample, the free electron energy spectrum is measured in a post-column EELS system with a spectrometer dispersion of  $\sim 0.1$  eV (Gatan). To reduce the isochromaticity effects we selected a smaller region of interest ( $< 15 \mu\text{m}$ , chosen by the wavepacket propagation distance) compared to the whole acquired image area ( $35 \times 35 \mu\text{m}$ ). The EELS system includes a slit for producing energy-filtered transmission electron microscopy (EFTEM) images. For each experiment, we choose the energy-filtering slit that maximizes the measured signal, thus reducing the sensitivity to the drift of the zero-loss peak during the measurement (typically  $\sim 0.25$  eV along  $\sim 1.5$  hours); see Fig. S4. This energy filtering optimization facilitated a typical acquisition time of 100 seconds per frame, creating a movie of the spatiotemporal dynamical in 100 minutes for a typical 60-frame measurement. Each slit choice alters the nonlinear relation between the electron signal and the electric field of the PhP wavepacket. The slit provides a sharp threshold above which the electric field can be measured, which is useful for eliminating secondary wavepackets due to the imperfections of the IR laser excitation (see Fig. S3).

### Sample preparation

Samples were fabricated by a variation of the viscoelastic polydimethylsiloxane (PDMS) dry transfer techniques (51,52). In the fabrication process, we mechanically exfoliate isotopically pure  $\text{h}^{11}\text{BN}$  crystals on viscoelastic PDMS tapes, commercially available from GELPAK. To reduce the amount of chemical residue and to conserve the hBN crystal, no tape was used in the exfoliation. Rather, exfoliation was performed directly with low retention PDMS (X0, in DGL or PF format). The original crystal was exfoliated until the PDMS was visibly covered in hBN all around, at which point a fresh PDMS sheet was used to pick up a portion of the hBN on the original PDMS, and then, further exfoliation could be performed.

After 2–5 such rounds, a last round of exfoliation was performed directly on the stamp, by attaching and separating it to one of the hBN covered PDMS sheets. By controlling the speed of the exfoliation, especially in this last step, we change the prevalent physical process; at slower speeds, flakes tend to move from one PDMS to another and at higher speeds they tend to exfoliate, but at the risk that they apply strain and crack or break the flakes.

To estimate the thickness of the hBN flakes on the stamp, we compared the optical contrast of a set of flakes, transferred them to a Si/SiO<sub>2</sub> chip, and measured, by atomic force microscope (Park NX20), the thickness of the hBN flakes. Based on these measurements and linear extrapolation, the on-stamp thickness can be estimated quickly and matched with good accuracy to the EELS log ratio measurement.

The flake is then transferred to the Si<sub>3</sub>N<sub>4</sub> membrane. We used commercially available 20 nm thick SiN<sub>x</sub> membranes (Norcada). A light oxygen plasma treatment was sometimes used to promote the flakes' tendency to stick to the membrane. To drop the flakes, the membrane was heated to 60° C , after which the PDMS was slowly brought into contact with the membrane window (see Fig. S7). We constantly tracked under an optical microscope the locations of the flake, the membrane window, and the contact front between the PDMS and the membrane's support substrate. The PDMS was then lifted extremely slowly, leaving the hBN attached to the Si<sub>3</sub>N<sub>4</sub>. In some cases, if the flake showed signs of not remaining connected to the membrane, the temperature was raised up to 90° C before the stamp was lifted.

#### Analysis of the measured PhP wavepacket

As the basis of our PhP wavepacket analysis, we assume that the coupling between the laser and the PhPs occurs at the sample's edge. There can be no coupling elsewhere, because the PhP momentum is larger than that of a free-space photon at the same frequency. This momentum mismatch forces a coupling through a spatial discontinuity, such as the edge of the sample. In our samples, the only discontinuity that can compensate the momentum mismatch and enable PhP coupling is the edge of the sample. The coupling can be modeled as if the laser induces a range of dipoles along the edge of the sample, which together excite both the propagating PhPs and edge modes (53). Using the side-illumination and the tilt of the sample (Fig. 1(a)), we can achieve conditions where the PhP is excited from only a single edge of the flake. Moreover, the laser excites the entire edge of the sample simultaneously and coherently to form a PhP wavepacket which propagates perpendicularly to the edge.

In the analysis of the measured PhP wavepacket, we initially apply an edge detection algorithm (Sobel) on the unfiltered electron image of the sample (Fig. S2(a-b)). Then, we extract the location and direction of the specific edge to which the PhP is coupled. After identifying the edge of interest, we start analyzing the filtered electron images. As shown in Fig. S2(c), we rotate

the images so that the edge is along the  $x$ -direction and the propagating direction is toward the minus  $y$ -direction and define the rectangular region that we aim to analyze (plotted in yellow). Note that in this figure the circular spot of the electron beam covers an area smaller than the screen, and therefore, it is focused to the area of interest to enhance the signal and reduce the integration time and isochromaticity within this region. Inside each rectangular region of interest, the signal-to-noise-ratio is largely reduced by averaging the signal along the edge ( $x$ -direction). Thus, we extract the resulting signal for different time delays (Fig. S2(d)). Notably, to analyze the evanescent decay of the field outside the sample, we normalize the counts outside the sample relative to the counts inside the sample. The difference in normalization arises from the scattering of electrons by the hBN flake. We account for this normalization difference using the difference in the number of electrons in the zero-loss peak inside and outside the sample. For the 55 nm sample, we find that this factor is 1.9.

Next, we analyze the signal in each time delay. We find that the measured wavepacket inside the sample can be accurately approximated by a Gaussian shape, as in Fig. S2(e), or by a double Gaussian, as in Fig. 4, with another exponential decay near the edge that correspond to the higher branches. The ability to fit the signal to a Gaussian allows us to find the wavepacket's central location as compared to the edge of the sample (through the Gaussian peak), shown in Fig. S2(f). The group velocity of the wavepacket is then extracted from a linear fit of the peak location over a range of time delays.

In addition to the peak location, the Gaussian shape enables us to examine the broadening over time and the overall wavepacket energy during its propagation, as plotted in Fig 3(e). In the plot, we show the wavepacket normalized integrated signal, calculated as  $I = \frac{1}{I_{\max}} ac \left( \operatorname{erf} \left( \frac{b}{\sqrt{2}c} \right) + 1 \right)$ , where  $a$ ,  $b$ , and  $c$  are the Gaussian's amplitude, center position (since the Gaussian can be truncated at the edge), and width (standard deviation), respectively.  $I_{\max}$  corresponds to the maximal energy during the measurement. Thus, the normalized integrated signal  $I/I_{\max}$  utilizes all the fitting parameters of the Gaussian. In addition, the wavepacket's integrated signal can help isolate the effects of the pumping pulse versus the decay caused by intrinsic polaritonic losses and dispersion broadening.

## Theory of the electron–polariton interaction using the generalized continuous-PINEM

In this section, we develop the theory of the PINEM interaction for a pulsed-laser excitation that has a significant bandwidth, so that the single-frequency PINEM theory (20, 21) is not sufficient. We obtain the frequency-dependent laser excitation as the output of the Finite-difference time-domain (FDTD) simulations (Lumerical). We find the frequency dependency of such excitations through a Fourier transform of the  $z$  component of the time-dependent electric field  $E_z(z, t)$ ,

$$E_z(z, \omega) = \mathcal{F}\{E_z(z, t)\}. \quad (\text{S1})$$

Under the commonly used PINEM approximations (20, 21), i.e., electron paraxiality and a small electron recoil in photon absorption/emission, we can use the continuous PINEM theory from (42). The theory defines a frequency-dependent PINEM coupling function (also Eq. (1) in the main text):

$$g(x, y, \omega) = \frac{e}{\hbar\omega} \int_{-\infty}^{\infty} dz E_z(x, y, z, \omega) e^{-i\frac{\omega}{v}z}, \quad (\text{S2})$$

where  $e$  and  $v$  are the electron charge and velocity, respectively, and  $\hbar$  is the reduced Planck's constant. Notice that the complex function  $g(x, y, \omega)$  has units of  $(\text{rad}/\text{sec})^{-1}$ , since its magnitude represents the spectral density of the interaction strength.

The frequency-dependent coupling coefficient enables us to derive the energy distribution of the post-interaction electron. The electron energy  $\Delta E$  is defined relative to its initial kinetic energy  $E_0 = m_0 c^2 \left(1 - \frac{1}{\sqrt{1-(v/c)^2}}\right)$ , where  $c$  is the speed of light and  $m_0$  is the bare electron mass. Using the above definition of  $g$ , we can write the post-interaction electron wavefunction in the energy domain as

$$f_e(x, y, \Delta E) = \frac{1}{2\pi\hbar} \int_{-\infty}^{\infty} dt e^{\frac{i\Delta E}{\hbar}t + 2i \int_0^{\infty} d\omega |g(x, y, \omega)| \sin(\omega t - \ar(g(x, y, \omega)))}. \quad (\text{S3})$$

Eq. (S3) assumes a monoenergetic electron ( $E_0$ ) before the interaction (generalized below to the realistic electron). The expression in Eq. (S3) shows that the typically required interaction strength for an observable signal is  $\int |g(\omega)| d\omega > 1$ , as found in the experiment. More precisely, the typical mean electron energy change is  $\int \hbar\omega |g(\omega)| d\omega$  and needs to be at least comparable to the width of the ZLP (0.9 eV). We note that in the special case of an excitation that is completely monochromatic, Eq. (S3) becomes a sum of Bessel functions as in the common PINEM theory.

Noticeably,  $f_e(x, y, \Delta E)$  incorporates the dependency on the spatial coordinates  $x, y$ , which carry the information about the PhP wavepacket profile at each point in time.

The realistic electron is pulsed, which is essential for the spatiotemporal measurement. Therefore, the pre-interaction electron is in fact a superposition of energy states, with a Gaussian envelope:

$$G(\Delta E, \tau_d) = \left(\frac{\sigma_t^2}{\pi}\right)^{\frac{1}{4}} e^{-\frac{\sigma_t^2}{2}\left(\frac{\Delta E}{\hbar}\right)^2} e^{-i\tau_d\frac{\Delta E}{\hbar}} \quad (\text{S4})$$

where  $\sigma_t$  is the initial electron time width and  $\tau_d$  is the time delay between the electron pulse and the laser pulse. As a result, we coherently convolve the distributions of Eqs. (S3) and (S4) to reach the total electron wavefunction in the energy domain,

$$f_{\text{total}}(x, y, \tau_d, \Delta E) = f_e(x, y, \Delta E) * G(\Delta E, \tau_d). \quad (\text{S5})$$

The expression in Eq. (S5) is the Fourier transform of the electron wavefunction in the time domain  $\phi_{\text{total}}(\vec{r}, t, \tau_d) = \int_{-\infty}^{\infty} f_{\text{total}}(x, y, \tau_d, \Delta E) e^{i\frac{\Delta E}{\hbar}(z-vt)} d\Delta E$ . We note that  $\phi_{\text{total}}$  contains the same modulation as Eq. (2) in the main text. The eventual electron energy distribution (measured in EELS) is  $|f_{\text{total}}|^2$  convolved with the incoherent electron energy width:

$$\rho(\Delta E, \tau_d) = |f_{\text{total}}(x, y, \tau_d, \Delta E)|^2 * \rho_{\text{ZLP}}(\Delta E) \quad (\text{S6})$$

where  $\rho_{\text{ZLP}}$  is the ZLP that describes the pre-interaction electron energy spectra. This expression can also be generalized to account for incoherent broadening in the time domain, by using the incoherent electron density in time and energy  $\rho_{\text{ZLP}}(t, \Delta E)$  and convolving over both time and energy. The overall electron pulse duration in our experiment is  $\sim 300$  fs.

Throughout the paper, we use the theory above to convert the electric field from the FDTD simulations into an EFTEM signal. The theory also enables to invert the process: to estimate the field strength from the measurement, by using the system parameters (e.g., electron velocity and energy slit), and other parameters such as the excitation laser frequency and PhP dispersion. The EFTEM signal depends on the field strength, frequency, confinement, electron velocity, and electron energy-filter cutoff. For calculating the electron-PhP coupling strength, at the parameter range in our experiment, we can approximate the PhP field as an anti-symmetric evanescent field,  $E_z(\omega) = \text{sign}(z)E_0 e^{-k_z|z|}$ , with  $k_z = \sqrt{q^2 - \omega^2/c^2}$  and  $q = q(\omega)$  being the real part of the PhP in-plane wavevector. We substitute the field into Eq. (S2) and find a Lorentzian response,

$$g(x, y, \omega) = E_0(x, y, \omega) \frac{2e}{\hbar\omega} \int_0^\infty dz e^{-k_z z} \sin\left(\frac{\omega}{v}z\right) = E_0(x, y, \omega) \frac{2e}{\hbar} \frac{v}{\omega^2 + (vk_z)^2}. \quad (\text{S7})$$

From Eq. (S7), we can infer that for a constant field amplitude  $E_0$ , modes with higher confinement (smaller  $k_z$ ) are harder to measure because  $g$  is smaller. We note that the higher branches remain visible despite stronger confinement, since  $E_0$  is larger when the PhP are more confined, which partially compensates for the weaker interaction at higher  $k_z$ . Finally, Eq. (S7) can help us to extract the PhP field strength in the experiment ( $1.5 \frac{MV}{m}$  for  $g = 8$ ,  $k_z = 1 \mu m^{-1}$ , and  $v = 0.7c$ ). We can also use this equation to deduce the optimal electron velocity for each polariton measurement,  $v_{opt} = \frac{\omega}{k_z}$ . For the 1<sup>st</sup> branch in the 55, 12, and 7.5 nm samples, we expect  $v_{opt} \cong 0.9c$ ,  $0.3c$ , and  $0.15c$  respectively. Generally, as the mode's confinement increases,  $v_{opt}$  decreases.

## Supplementary text

### Comparison of PINEM and other nearfield imaging techniques

It is valuable to discuss our PINEM-based experimental capabilities in light of the state of the art in nearfield optical microscopy of 2D polaritons. In the visible and near-IR regimes, recent studies compared the PINEM capabilities with other nearfield imaging techniques (27,35,54). The prospects of PINEM that were developed over the last decade now become of greater value when applied to the challenge of imaging 2D polaritons in the mid-IR: specifically, the electron penetration, non-destructive interaction, fs time resolution, and deep subwavelength spatial resolution, all of which are especially advantageous for the unique circumstances of 2D polaritons. In comparison with SNOM, the most influential technique in the field of 2D polaritons (6, 17, 18, 30), our approach images the field in a non-destructive manner. That is, the electrons perform a “passive” measurement that can record the flow of light without altering it, as can occur when nearfield microscope tips are used. Moreover, since the electron probes the field inside the sample, it is not necessary to outcouple the light, and thus, the signal from higher PhP branches increases dramatically. For this reason, all branches experience similar detection efficiencies as that of the first-branch PhP, though most of the higher branches are measured as an exponential decay near the edge.

We envision future experiments in which free electron probes are used for record-high spatial resolution in nearfield optical microscopy, reaching single-nm resolutions and below

(considered beyond the reach of conventional nearfield imaging tips used in SNOMs). Single-nm resolutions are of great importance for imaging polaritons of the highest confinement (e.g., Ref. (40)), where new physics can emerge, such as the effects of optical nonlocality. The features in the PhP wavepacket in our experiment were not sufficiently small to test this limit. A disadvantage of the current PINEM approach is that the pulsed free electron does not sense the PhP phase since it is averaged-out over the electron pulse duration ( $\sim 300$  fs). To measure the propagating wavepacket phase as in SNOM, one could consider interference between two polaritons (26), shorter electron pulse durations, or pre-bunched electrons, which were already shown to reach attosecond timescales in electron microscopes (25, 55). Using attosecond electron probes would open the possibility to measure the dynamics of plasmon polariton wavepackets in the visible range.

Direct imaging of 2D polariton wavepacket dynamics could be considered in several other nearfield imaging techniques that so far were not applied to the mid-IR frequencies, such as time-resolved photon tunneling microscopy (56) and time-resolved photo-emission electron microscopy (TR-PEEM) (57,58), which were used for the analysis and the design of plasmonic nanocircuits (59). Historically, the first method used to image the dynamics of propagating polaritons was based on optical nonlinearities in the materials in which the polaritons propagated, specifically the electro-optic effect (60, 61). It could be interesting to consider this approach for the observation of wavepacket dynamics in 2D materials, especially in light of recent research on optical nonlinearities in 2D materials (43).

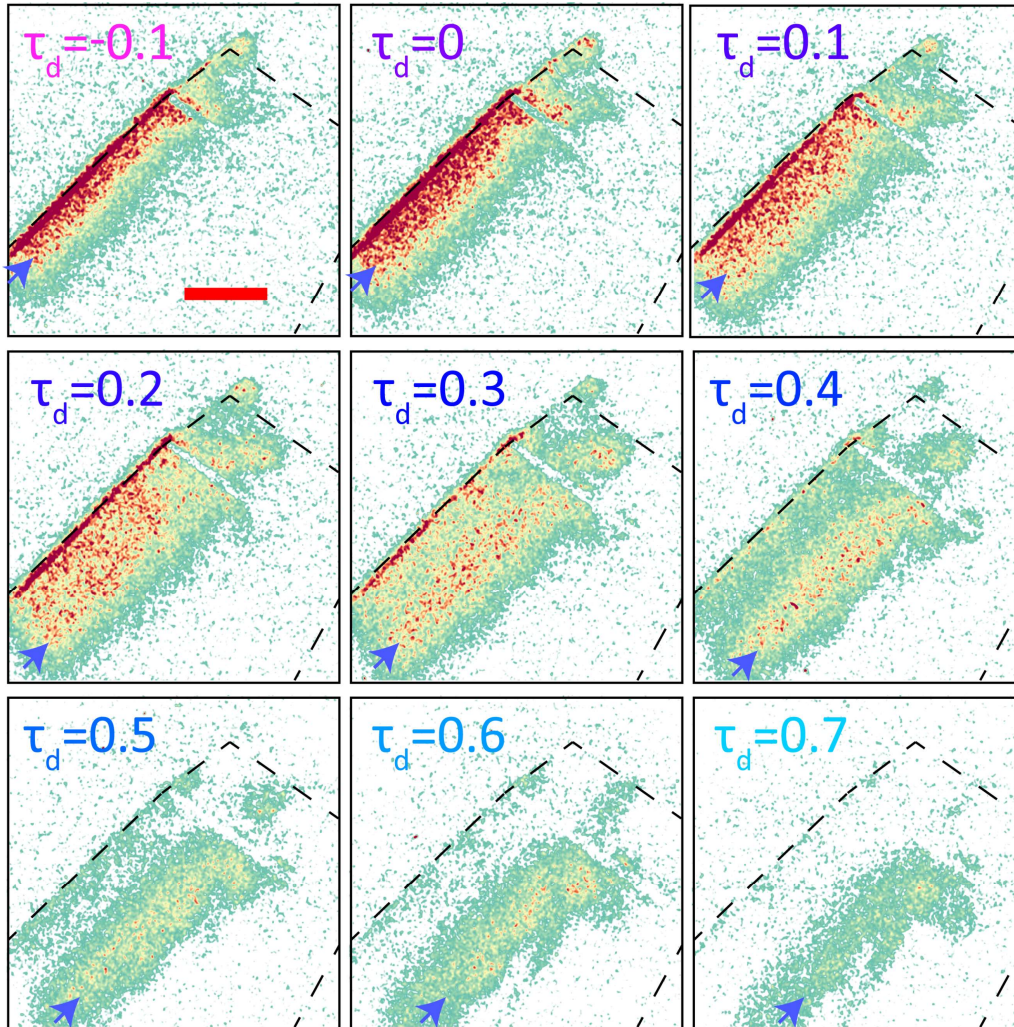


**Fig. S1. Energy-filtered electron images in different time delays: showing the propagation of a polariton wavepacket in a flake of hBN.** The sample borders are marked by dashed lines, and the wavepacket's peak location by a blue arrow. The times are in units of ps. These images are the top view of Fig. 1(d), and the average signal along the edge of the sample corresponds to Fig. 2(a).

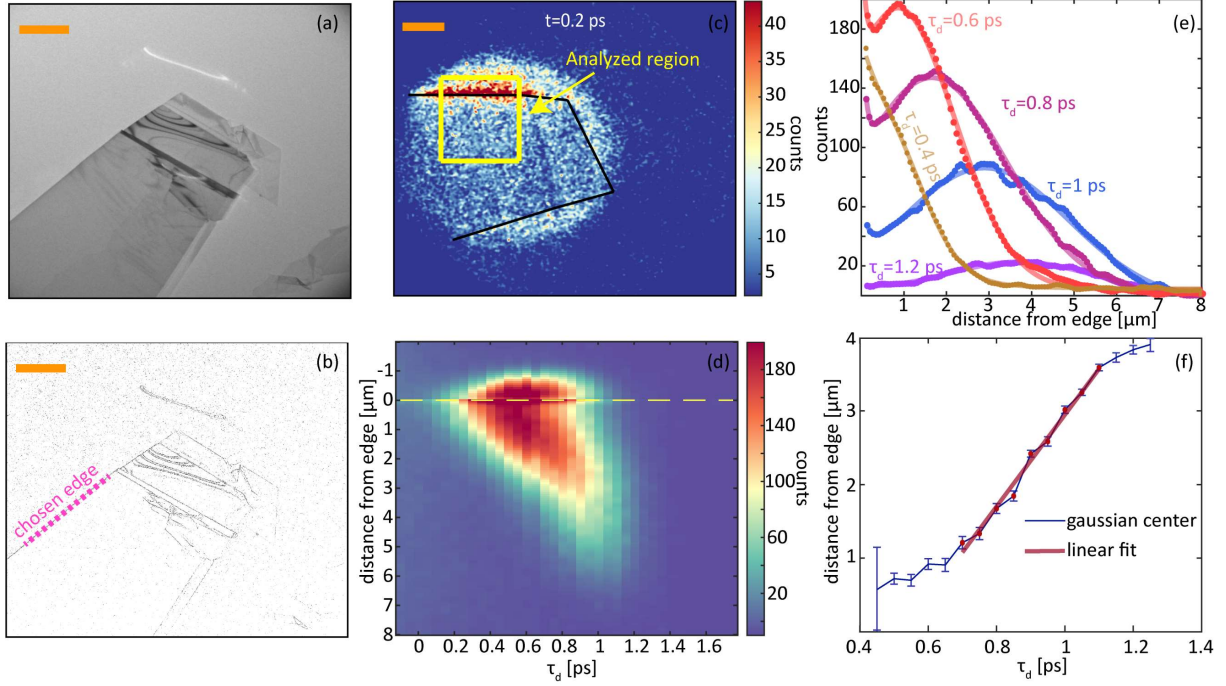


**Fig. S2: Extraction of the group velocities from measurements.** (a) TEM image of the h<sup>11</sup>BN sample without electron energy filtering. (b) Edge detection of the sample obtained by applying the Sobel algorithm to (a). We manually choose the edge in which we analyze the phonon-polariton (PhP) propagation, depicted by the dashed pink line. (c) Energy-filtered image at 0.2 ps after the initial arrival of the laser pulse, rotated so that the PhP propagation direction is along one of the image axes (sample borders in black). We then choose the analyzed region (yellow) in which we average the signal along the  $x$ -axis of the image. In this case, the yellow region width and height are  $9.3 \times 10 \mu\text{m}$ , which are  $115 \times 124$  pixels. We analyzed the propagation along the  $y$ -axis. The orange scales in panels (a-c) denote  $5 \mu\text{m}$ . (d) Averaged signal as a function of time delay  $\tau_d$  and distance from the chosen edge (yellow dashed line). (e) Signal from (d) at specific times  $\tau_d$ , including the Gaussian fits of each curve. The fit includes a Gaussian plus an exponential decay to include the higher-order modes and edge-effects. (f) Group velocity extraction through a linear fit of the Gaussian peak location, as a function of the time delay (blue). For the fit, we exclude early times (below 0.7 ps) in which the wavepacket is still accelerating. In addition, we exclude late times (above 1.1 ps) in which the wavepacket experiences a deceleration. The group velocity in this measurement is found to be  $v_g = 5.5 \pm 0.35 \frac{\mu\text{m}}{\text{ps}}$ .

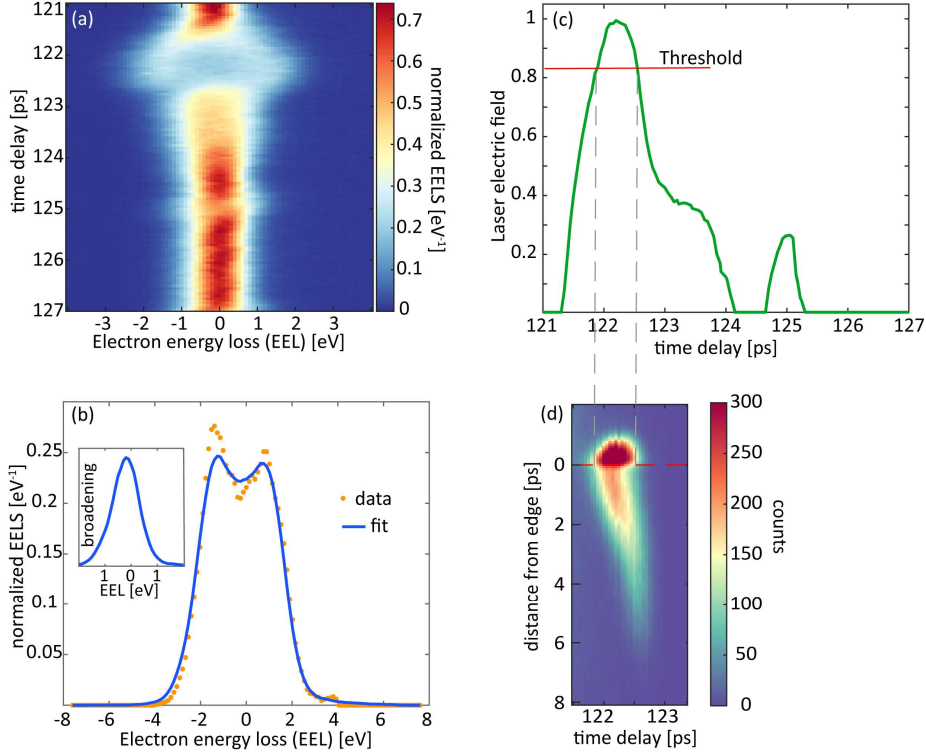


**Fig. S3: Extraction of the laser pulse excitation temporal profile.** (a) The pulse duration at each DFG center-wavelength (shown here for 6980 nm) was measured using a PINEM-type pump-probe experiment on an independent sample (aluminum foil). The panel shows the map of electron energy loss spectra (EELS) as a function of time delays  $\tau_d$  between the excitation laser pulse and the electron pulse, normalized so that the energy integral is unity  $\int EELS(\tau_d, E)dE = 1$  for each time delay. (b) Normalized EELS measured data (orange) and fit (blue). In the fit, we extract a single fitting parameter for each delay  $\tau_d$ , the PINEM coupling  $\int d\omega g(\omega, \tau_d)$ , from which we extract the PhP electric field intensity. The EELS is calculated by convolving the electron energy width (zero-loss-peak, shown in inset, measured with no laser) with the PINEM discrete spectra:  $EELS(\Delta E, \tau_d) = \rho_{ZLP}(\Delta E) * \sum_n |J_n(2 \int d\omega g(\omega, \tau_d))|^2 \delta(\Delta E - n\hbar\omega)$  with  $J_n$  being the Bessel function. In this case,  $\hbar\omega = 0.18$  eV, the time delay  $\tau_d$  is 122.5 ps, and the integrated coupling is found to be  $\int d\omega g(\omega, \tau_d) = 6.12$  at the peak of the envelope. By repeating this fitting algorithm for each  $\tau_d$ , we reconstruct the entire laser pulse profile. (c) The reconstructed electric field of the laser pulse as a function of time delay, normalized to its maximal value. This electric field is linear with  $g$ , with the same pre-factor for all time delays. The red vertical line represents the field threshold that can cause a PhP measurement for the slit that is chosen in the measurement in (d). The field profile was reshaped by interactions with vibrational water molecules in air, which also create a chirp (46). (d) A map showing the dynamics of the PhP wavepacket. The same data from Fig. S2 (d), presented here to highlight the correspondence to the laser excitation in (c). The slit that we chose imposes the field threshold represented by a red line in (c). The characteristics of the laser excitation in each measurement of Fig. 3 were measured in a manner similar to that presented here.

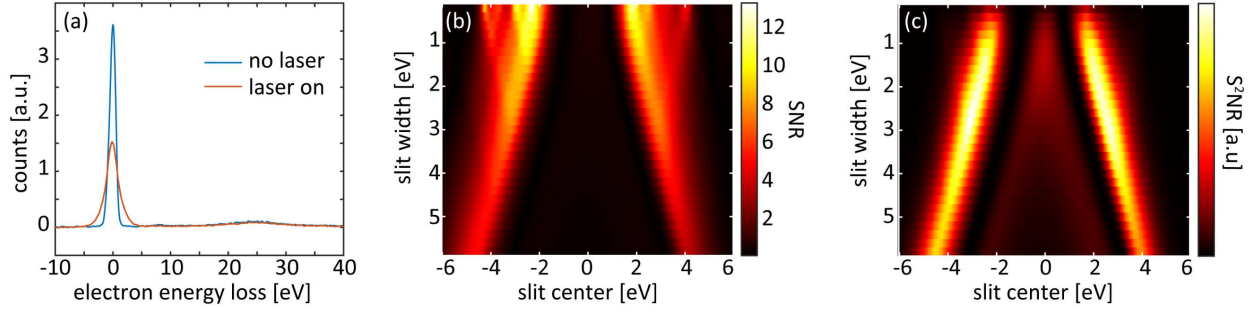


**Fig. S4: Effect of the energy filtering slit. (a)** Electron energy loss with (orange) and without (blue) the IR laser. **(b)** Signal-to-noise ratio (SNR) as a function of the slit width and its center location. The center of the slit is chosen relative to the location of the electron ZLP. As in EELS, the minus sign is related to gain. The SNR is defined as  $\frac{\int d(\Delta E)[W(\Delta E)|EELS_L(\Delta E) - EELS_N(\Delta E)|]}{\int d(\Delta E)[W(\Delta E)|EELS_N(\Delta E)|]}$ , where  $W$  is the slit window and  $EELS_{L,N}$  is the EELS when the laser is on and off, respectively. **(c)** Squared-signal-to-noise ratio ( $S^2NR$ ) that we define here as  $\frac{\int d(\Delta E)[W(\Delta E)|EELS_L(\Delta E) - EELS_N(\Delta E)|^2]}{\int d(\Delta E)[W(\Delta E)|EELS_N(\Delta E)|]}$ . This ratio gives additional weight to the number of electrons that are involved in the interaction and thus combines the signal-to-noise ratio with a minimization of the integration time. In all our measurements, we chose the slit that maximizes the  $S^2NR$ , a method we found to provide a good indication for signal quality optimization. Importantly, the optimized  $S^2NR$  optimization provides better measurement stability, reducing the sensitivity to the drift of the zero-loss peak during the measurements. In this specific example, the optimal slit is centered at -3.05 eV and with a width of 2.8 eV.

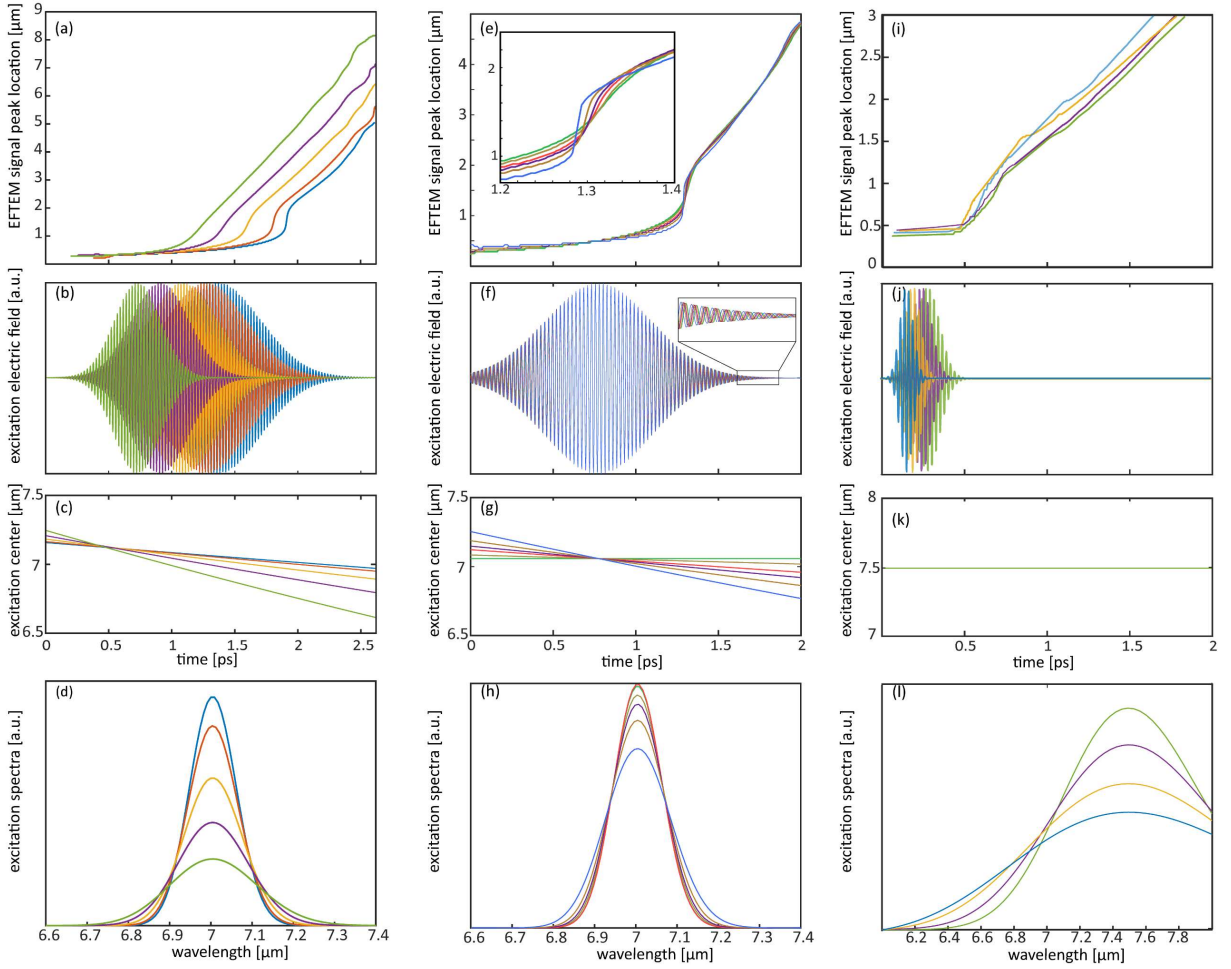


**Fig. S5. Numerical simulations that show the acceleration-deceleration phenomena – abrupt changes in the group velocity.** The numerical simulation models the entire experiment from the PhP excitation and propagation (Lumerical), through the continuous-PINEM interaction (Eq. (S6)), to the energy filtering with EFTEM, resulting in the measured electron signal. **(a)** Wavepacket peak location according to our numerical simulation in a 55 nm sample. The different curves correspond to varying different excitation properties: the pulse duration **(b)**, chirp **(c)**, and spectra **(d)**. In the set of simulations shown in panel (a), we varied the pulse duration and its chirp while retaining a fixed central wavelength of  $7 \mu\text{m}$ . The conclusion we draw from (a-d) is that as the pulse duration increases, the group velocity becomes less stable and shows more abrupt acceleration and deceleration. **(e)** Same as (a) with the corresponding excitation properties shown in **(f-h)**. In this set of simulations, we varied the chirp while fixing the pulse duration. The insets in (e) and (f) correspond to a zoom-in of the corresponding figures. The conclusion we draw from (e-h) is that, as the chirp increases, the group velocity shows stronger acceleration and deceleration. **(i)** Wavepacket peak location according to our numerical simulation for a 20 nm sample with the corresponding excitation properties shown in **(j-l)**. In this set of simulations, we varied the bandwidth and pulse duration of the excitation while fixing the pulse chirp and central wavelength. The conclusion we draw from (i-l) is that a deceleration in the group velocities can occur also without a chirp, but with a broadband excitation.

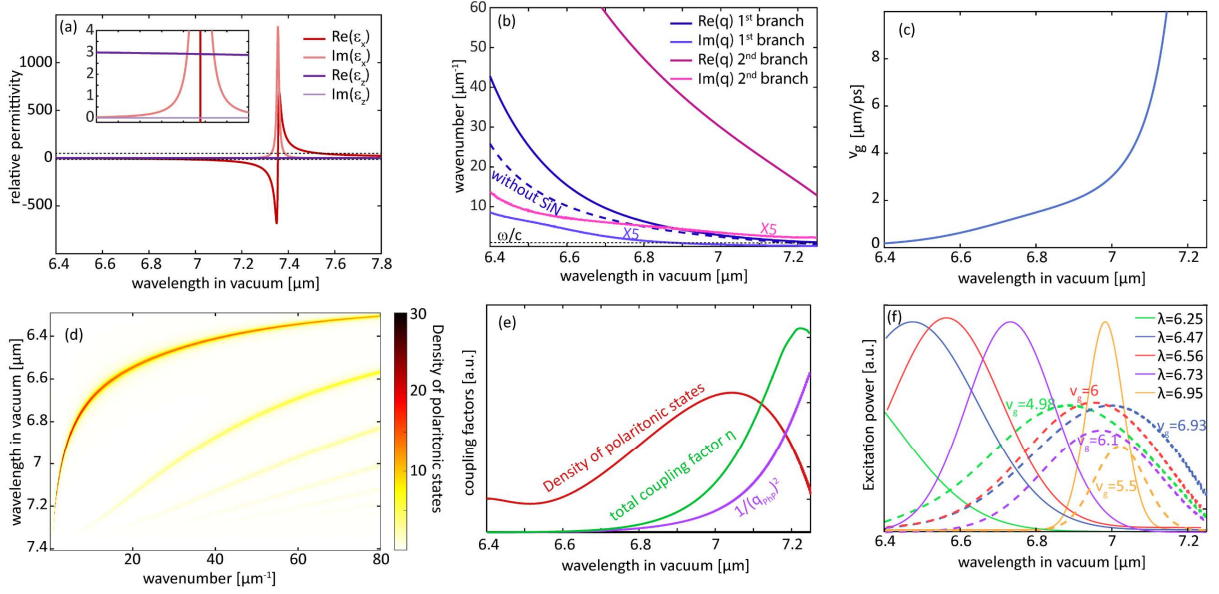


**Fig. S6. Theoretical modeling of PhPs in hBN.** (a) The imaginary and real part of each permittivity component of an isotopically pure hBN (<sup>11</sup>B) flake. (b) The real and imaginary parts of the PhP in-plane wavevector  $q$  in an hBN sample with thickness of 55 nm. The dashed line corresponds to  $\text{Re}(q)$  of the 1<sup>st</sup> mode when neglecting the 20 nm Si<sub>3</sub>N<sub>4</sub> membrane, showing that the membrane cannot be neglected when modeling PhP modes of higher energies and wavevectors. Interestingly, although  $\text{Im}(q)$  is larger for the second branch, its quality factor,  $Q = \text{Re}(q)/\text{Im}(q)$ , is larger than the first branch since the ratio  $\frac{v_{\text{phase}}v_g}{c^2}$  of the second branch is larger. (c) Group velocity of the first PhP mode as a function of excitation wavelength. (d) The density of polaritonic states, showing the different PhP branches. (e) Coupling factors between the free-space photons and the PhP as a function of wavelength. The total coupling factor  $\eta(\lambda)$  (green) is a multiplication of the polaritonic density of states (red) by the inverse squared of the polariton momenta  $q_{\text{PhP}}$  (purple). (f) Excitation spectra of the pulses for different DFG central-wavelengths. The solid curves show the excitation spectra in vacuum  $S(\lambda)$ , as estimated from a Michelson interferometer setup. The dashed lines represent the effective PhP excitation spectra  $S_{\text{eff}}(\lambda)$  calculated using a multiplication of the total coupling factor by the excitation spectra in vacuum, that is,  $S_{\text{eff}}(\lambda) = S(\lambda)\eta(\lambda)$ . These effective excitation spectra enable us to calculate a weighted average of the group velocity through  $v_g = \int S_{\text{eff}}(\lambda)v_g(\lambda)d\lambda$ . The group velocities calculated using this method are all within the errors of the measured velocities (as shown in Fig. 3).

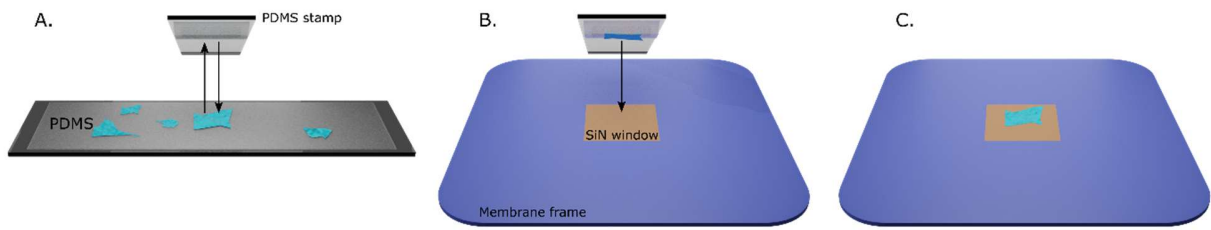


**Fig. S7: Sample preparation – steps of the dry transfer process. (a)** Pickup from the exfoliating PDMS sheet by using a PDMS stamp. **(b)** A slow release of the flakes from the stamp to the  $\text{Si}_3\text{N}_4$  membrane. **(c)** The remaining flake after the stamp was removed.

**Table S1: Excitation laser parameters.** The laser pulses at the DFG output were characterized spectrally through a Michelson interferometer.

Sample	Plot color in Fig. 3	Central wavelength [nm]	Standard deviation [nm]	Group velocity $\left[\frac{\mu\text{m}}{\text{ps}}\right]$
7.5 nm	green	7140	60	$0.87 \pm 0.043$
	Blue	6850	120	$0.84 \pm 0.16$
	Bright blue	6680	115	$0.35 \pm 0.16$
12 nm	Yellow	7060	80	$1.07 \pm 0.03$
	Dark red	6800	115	$1.3 \pm 0.06$
55 nm	red	6980	50	$5.5 \pm 0.35$
	Green	6730	115	$6.1 \pm 0.16$
	Blue	6560	150	$6 \pm 0.18$
	Purple	6470	175	$6.7 \pm 0.48$
	yellow	6250	190	$4.9 \pm 0.47$

## Captions for Movies S1 to S4

**Movie S1. Video showing the evolution dynamics of a PhP wavepacket.** The video is composed of energy-filtered electron measurements with varying time delays. When the laser pump illuminates the left edge of the sample, the wavepacket is formed and propagates toward the right side of the sample. Here, the wavepacket is formed and remains “stuck” near the edge until a time delay of 122.25 ps. Then, as the pump decays (estimated by the signal outside the sample), the wavepacket begins to propagate along the sample and finally decays at a time delay of approximately 123.25 ps. Bottom inset: image of the sample, acquired without energy filtering of the electrons. Top inset: wavepacket’s signal averaged parallel to the sample’s edge versus the distance from the edge.

**Movie S2. Video showing the evolution dynamics of a multi-branch PhP wavepacket.** The video is composed of energy-filtered electron measurements with varying time delays. When the laser pump illuminates the left edge of the sample, the wavepacket is formed and propagates toward the right side of the sample. Here, a multi-mode wavepacket is formed, which then splits into two distinct wavepackets (at delay time of 122.4 ps) having different group velocities. At time 123.1 ps, a second pulse begins triggering a second excitation at the left edge of the sample, while the first wavepacket still propagates and reaches the right edge. Bottom inset: image of the sample, acquired without energy filtering of the electrons. Top inset: wavepacket’s signal averaged parallel to the sample’s edge versus the distance from the edge.

**Movie S3. Simulation of wavepacket dynamics with long-pulse excitation.** (a) FDTD simulation of the  $z$  component of the electric field in a 55 nm thick, isotopically pure hBN flake on top of a 20 nm  $\text{Si}_3\text{N}_4$  membrane. (b) Excitation field profile as a function of time. A red dot denotes the field at each time delay  $\tau_d$  (between the electron pulse and excitation laser pulse). The excitation used in the simulation is a dipole located on the left side of the sample. (c) Excitation wavelength over time, showing the chirped profile of the excitation dipole. (d) EFTEM signal, calculated based on the field in (a), extracted using the continuous-PINEM theory in the Materials and Methods. (e)  $z$  component of the electric field at the surface of the hBN sample, related to an SNOM measurement. (f) Wavepacket location (using the Gaussian fitting for each time point) according to the free-electron probe signal (blue) and the expected SNOM signal (orange). The comparative analysis of the two approaches provides similar results and a similar estimated group velocity.

This simulation shows the S-trajectory, similar to that observed in some of our experiments. Thus, the simulation helps explain the dynamics during the three stages of the wavepacket propagation. In the first stage ( $<0.4$  ps), the laser excitation is still on and the wavepacket remains near the edge (having an extremely slow group velocity). In the second stage ( $\sim 0.4$  ps– $0.6$  ps), the wavepacket propagates away from the edge at a relatively high group velocity for a limited time span, occurring while the tail of the excitation pulse has not yet ended. In the third stage ( $>0.6$  ps), the excitation pulse has mostly ended and deceleration occurs, and therefore, the wavepacket reaches its steady group velocity. We observe the dynamics of acceleration followed by deceleration only when the excitation pulse is sufficiently long that the wavepacket already starts to propagate before the excitation pulse ends. In that case, we see two parts of the wavepacket combine, creating a temporary flat profile (at about 0.54 ps), which creates the impression of a high group velocity.

Note that at some measurements, the first stage was not resolved; thus, it appears that there is only an effect of deceleration, which is fully explained by a transition from the second to the third stage.

**Movie S4: Simulation of wavepacket dynamics with short-pulse excitation.** (a) FDTD simulation of the  $z$  component of the electric field in a 55 nm thick, isotopically pure hBN flake, on top of a 20 nm  $\text{Si}_3\text{N}_4$  membrane. (b) Excitation field profile as a function of time. A red dot represents the field at each time delay  $\tau_d$  (between the electron pulse and excitation laser pulse). The excitation used in the simulation is a dipole located on the left side of the sample. (c) Excitation wavelength over time, showing the chirped profile of the excitation dipole. (d) EFTEM signal, calculated based on the field in (a), extracted using the continuous-PINEM theory in the SM. (e)  $z$  component of the electric field at the surface of the hBN sample, related to an SNOM measurement. (f) Wavepacket location (using the Gaussian fitting for each time point) according to the free-electron probe signal (blue) and the expected SNOM signal (orange). Unlike in Supplementary video 2, here the comparative analysis of the two methods provides different group velocities, which arise from the fact that the different probing methods weight each frequency component differently.

This simulation shows the reduced-S trajectory, similar to that observed in some of our experiments. Thus, the simulation helps explain the dynamics during the two stages of the wavepacket propagation. In the first stage ( $<0.4$  ps), the laser excitation is still on, and the wavepacket remains near the edge (having an extremely slow group velocity), as in Movie S2. In the second stage ( $>0.4$  ps), the excitation pulse has mostly ended, and therefore, the wavepacket reaches its steady group velocity. We observe this acceleration dynamics when the wavepackets do not propagate considerably until the end of the excitation pulse.

## References and Notes

1. M. Jablan, H. Buljan, M. Soljagic, Plasmonics in graphene at infrared frequencies. *Phys. Rev. B* **80**, 245435 (2009). [doi:10.1103/PhysRevB.80.245435](https://doi.org/10.1103/PhysRevB.80.245435)
2. D. N. Basov, A. Asenjo-Garcia, P. J. Schuck, X. Zhu, A. Rubio, Polariton panorama. *Nanophotonics* **10**, 549–577 (2020). [doi:10.1515/nanoph-2020-0449](https://doi.org/10.1515/nanoph-2020-0449)
3. V. W. Brar, M. C. Sherrott, D. Jariwala, Emerging photonic architectures in two-dimensional opto-electronics. *Chem. Soc. Rev.* **47**, 6824–6844 (2018). [doi:10.1039/C8CS00206A](https://doi.org/10.1039/C8CS00206A) [Medline](#)
4. P. Li, M. Lewin, A. V. Kretinin, J. D. Caldwell, K. S. Novoselov, T. Taniguchi, K. Watanabe, F. Gaussmann, T. Taubner, Hyperbolic phonon-polaritons in boron nitride for near-field optical imaging and focusing. *Nat. Commun.* **6**, 7507 (2015). [doi:10.1038/ncomms8507](https://doi.org/10.1038/ncomms8507) [Medline](#)
5. K. Chaudhary, M. Tamagnone, M. Rezaee, D. K. Bediako, A. Ambrosio, P. Kim, F. Capasso, Engineering phonon polaritons in van der Waals heterostructures to enhance in-plane optical anisotropy. *Sci. Adv.* **5**, eaau7171 (2019). [doi:10.1126/sciadv.aau7171](https://doi.org/10.1126/sciadv.aau7171) [Medline](#)
6. A. J. Giles, S. Dai, I. Vurgaftman, T. Hoffman, S. Liu, L. Lindsay, C. T. Ellis, N. Assefa, I. Chatzakis, T. L. Reinecke, J. G. Tischler, M. M. Fogler, J. H. Edgar, D. N. Basov, J. D. Caldwell, Ultralow-loss polaritons in isotopically pure boron nitride. *Nat. Mater.* **17**, 134–139 (2018). [doi:10.1038/nmat5047](https://doi.org/10.1038/nmat5047) [Medline](#)
7. D. Alcaraz Iranzo, S. Nanot, E. J. C. Dias, I. Epstein, C. Peng, D. K. Efetov, M. B. Lundberg, R. Parret, J. Osmond, J.-Y. Hong, J. Kong, D. R. Englund, N. M. R. Peres, F. H. L. Koppens, Probing the ultimate plasmon confinement limits with a van der Waals heterostructure. *Science* **360**, 291–295 (2018). [doi:10.1126/science.aar8438](https://doi.org/10.1126/science.aar8438) [Medline](#)
8. W. Ma, P. Alonso-González, S. Li, A. Y. Nikitin, J. Yuan, J. Martín-Sánchez, J. Taboada-Gutiérrez, I. Amenabar, P. Li, S. Vélez, C. Tollan, Z. Dai, Y. Zhang, S. Sriram, K. Kalantar-Zadeh, S.-T. Lee, R. Hillenbrand, Q. Bao, In-plane anisotropic and ultralow-loss polaritons in a natural van der Waals crystal. *Nature* **562**, 557–562 (2018). [doi:10.1038/s41586-018-0618-9](https://doi.org/10.1038/s41586-018-0618-9) [Medline](#)
9. Y. Kurman, I. Kaminer, Tunable bandgap renormalization by nonlocal ultra-strong coupling in nanophotonics. *Nat. Phys.* **16**, 868–874 (2020). [doi:10.1038/s41567-020-0890-0](https://doi.org/10.1038/s41567-020-0890-0)
10. N. Rivera, I. Kaminer, Light–matter interactions with photonic quasiparticles. *Nat. Rev. Phys.* **2**, 538–561 (2020). [doi:10.1038/s42254-020-0224-2](https://doi.org/10.1038/s42254-020-0224-2)
11. I. Epstein, D. Alcaraz, Z. Huang, V.-V. Pusapati, J.-P. Hugonin, A. Kumar, X. M. Deputy, T. Khodkov, T. G. Rappoport, J.-Y. Hong, N. M. R. Peres, J. Kong, D. R. Smith, F. H. L. Koppens, Far-field excitation of single graphene plasmon cavities with ultracompressed mode volumes. *Science* **368**, 1219–1223 (2020). [doi:10.1126/science.abb1570](https://doi.org/10.1126/science.abb1570) [Medline](#)
12. A. M. Weiner, Femtosecond pulse shaping using spatial light modulators. *Rev. Sci. Instrum.* **71**, 1929–1960 (2000). [doi:10.1063/1.1150614](https://doi.org/10.1063/1.1150614)

13. P. Colman, C. Husko, S. Combrié, I. Sagnes, C. W. Wong, A. De Rossi, Temporal solitons and pulse compression in photonic crystal waveguides. *Nat. Photonics* **4**, 862–868 (2010). [doi:10.1038/nphoton.2010.261](https://doi.org/10.1038/nphoton.2010.261)
14. M. A. Noginov, Y. A. Barnakov, G. Zhu, T. Tumkur, H. Li, E. E. Narimanov, Bulk photonic metamaterial with hyperbolic dispersion. *Appl. Phys. Lett.* **94**, 151105 (2009). [doi:10.1063/1.3115145](https://doi.org/10.1063/1.3115145)
15. A. Poddubny, I. Iorsh, P. Belov, Y. Kivshar, Hyperbolic metamaterials. *Nat. Photonics* **7**, 948–967 (2013). [doi:10.1038/nphoton.2013.243](https://doi.org/10.1038/nphoton.2013.243)
16. K. V. Sreekanth, A. De Luca, G. Strangi, Negative refraction in graphene-based hyperbolic metamaterials. *Appl. Phys. Lett.* **103**, 023107 (2013). [doi:10.1063/1.4813477](https://doi.org/10.1063/1.4813477)
17. S. Dai, Z. Fei, Q. Ma, A. S. Rodin, M. Wagner, A. S. McLeod, M. K. Liu, W. Gannett, W. Regan, K. Watanabe, T. Taniguchi, M. Thiemens, G. Dominguez, A. H. Castro Neto, A. Zettl, F. Keilmann, P. Jarillo-Herrero, M. M. Fogler, D. N. Basov, Tunable phonon polaritons in atomically thin van der Waals crystals of boron nitride. *Science* **343**, 1125–1129 (2014). [doi:10.1126/science.1246833](https://doi.org/10.1126/science.1246833) [Medline](#)
18. E. Yoxall, M. Schnell, A. Y. Nikitin, O. Txoperena, A. Woessner, M. B. Lundeberg, F. Casanova, L. E. Hueso, F. H. L. Koppens, R. Hillenbrand, Direct observation of ultraslow hyperbolic polariton propagation with negative phase velocity. *Nat. Photonics* **9**, 674–678 (2015). [doi:10.1038/nphoton.2015.166](https://doi.org/10.1038/nphoton.2015.166)
19. B. Barwick, D. J. Flannigan, A. H. Zewail, Photon-induced near-field electron microscopy. *Nature* **462**, 902–906 (2009). [doi:10.1038/nature08662](https://doi.org/10.1038/nature08662) [Medline](#)
20. F. J. García de Abajo, A. Asenjo-García, M. Kociak, Multiphoton absorption and emission by interaction of swift electrons with evanescent light fields. *Nano Lett.* **10**, 1859–1863 (2010). [doi:10.1021/nl100613s](https://doi.org/10.1021/nl100613s) [Medline](#)
21. S. T. Park, M. Lin, A. H. Zewail, Photon-induced near-field electron microscopy (PINEM): Theoretical and experimental. *New J. Phys.* **12**, 123028 (2010). [doi:10.1088/1367-2630/12/12/123028](https://doi.org/10.1088/1367-2630/12/12/123028)
22. D. T. Valley, V. E. Ferry, D. J. Flannigan, Imaging intra- and interparticle acousto-plasmonic vibrational dynamics with ultrafast electron microscopy. *Nano Lett.* **16**, 7302–7308 (2016). [doi:10.1021/acs.nanolett.6b03975](https://doi.org/10.1021/acs.nanolett.6b03975) [Medline](#)
23. T. T. A. Lummen, R. J. Lamb, G. Berruto, T. LaGrange, L. Dal Negro, F. J. García de Abajo, D. McGrouther, B. Barwick, F. Carbone, Imaging and controlling plasmonic interference fields at buried interfaces. *Nat. Commun.* **7**, 13156 (2016). [doi:10.1038/ncomms13156](https://doi.org/10.1038/ncomms13156) [Medline](#)
24. D. R. Cremons, D. A. Plemmons, D. J. Flannigan, Femtosecond electron imaging of defect-modulated phonon dynamics. *Nat. Commun.* **7**, 11230 (2016). [doi:10.1038/ncomms11230](https://doi.org/10.1038/ncomms11230) [Medline](#)
25. Y. Morimoto, P. Baum, Diffraction and microscopy with attosecond electron pulse trains. *Nat. Phys.* **14**, 252–256 (2018). [doi:10.1038/s41567-017-0007-6](https://doi.org/10.1038/s41567-017-0007-6)
26. I. Madan, G. M. Vanacore, E. Pomarico, G. Berruto, R. J. Lamb, D. McGrouther, T. T. A. Lummen, T. Latychevskaia, F. J. García de Abajo, F. Carbone, Holographic imaging of electromagnetic fields via electron-light quantum interference. *Sci. Adv.* **5**, eaav8358 (2019). [doi:10.1126/sciadv.aav8358](https://doi.org/10.1126/sciadv.aav8358) [Medline](#)

27. K. Wang, R. Dahan, M. Shentcis, Y. Kauffmann, A. Ben Hayun, O. Reinhardt, S. Tsesses, I. Kaminer, Coherent interaction between free electrons and a photonic cavity. *Nature* **582**, 50–54 (2020). [doi:10.1038/s41586-020-2321-x](https://doi.org/10.1038/s41586-020-2321-x) [Medline](#)
28. O. Kfir, H. Lourenço-Martins, G. Storeck, M. Sivis, T. R. Harvey, T. J. Kippenberg, A. Feist, C. Ropers, Controlling free electrons with optical whispering-gallery modes. *Nature* **582**, 46–49 (2020). [doi:10.1038/s41586-020-2320-y](https://doi.org/10.1038/s41586-020-2320-y) [Medline](#)
29. See supplementary materials.
30. R. Hillenbrand, T. Taubner, F. Keilmann, Phonon-enhanced light matter interaction at the nanometre scale. *Nature* **418**, 159–162 (2002). [doi:10.1038/nature00899](https://doi.org/10.1038/nature00899) [Medline](#)
31. M. A. Huber, F. Mooshammer, M. Plankl, L. Viti, F. Sandner, L. Z. Kastner, T. Frank, J. Fabian, M. S. Vitiello, T. L. Cocker, R. Huber, Femtosecond photo-switching of interface polaritons in black phosphorus heterostructures. *Nat. Nanotechnol.* **12**, 207–211 (2017). [doi:10.1038/nnano.2016.261](https://doi.org/10.1038/nnano.2016.261) [Medline](#)
32. M. Mrejen, L. Yadgarov, A. Levanon, H. Suchowski, Transient exciton-polariton dynamics in WSe<sub>2</sub> by ultrafast near-field imaging. *Sci. Adv.* **5**, eaat9618 (2019). [doi:10.1126/sciadv.aat9618](https://doi.org/10.1126/sciadv.aat9618) [Medline](#)
33. A. J. Sternbach, S. H. Chae, S. Latini, A. A. Rikhter, Y. Shao, B. Li, D. Rhodes, B. Kim, P. J. Schuck, X. Xu, X.-Y. Zhu, R. D. Averitt, J. Hone, M. M. Fogler, A. Rubio, D. N. Basov, Programmable hyperbolic polaritons in van der Waals semiconductors. *Science* **371**, 617–620 (2021). [doi:10.1126/science.abe9163](https://doi.org/10.1126/science.abe9163) [Medline](#)
34. B. Frank, P. Kahl, D. Podbiel, G. Spektor, M. Orenstein, L. Fu, T. Weiss, M. Horn-von Hoegen, T. J. Davis, F.-J. Meyer Zu Heringdorf, H. Giessen, Short-range surface plasmonics: Localized electron emission dynamics from a 60-nm spot on an atomically flat single-crystalline gold surface. *Sci. Adv.* **3**, e1700721 (2017). [doi:10.1126/sciadv.1700721](https://doi.org/10.1126/sciadv.1700721) [Medline](#)
35. A. Polman, M. Kociak, F. J. García de Abajo, Electron-beam spectroscopy for nanophotonics. *Nat. Mater.* **18**, 1158–1171 (2019). [doi:10.1038/s41563-019-0409-1](https://doi.org/10.1038/s41563-019-0409-1) [Medline](#)
36. R. F. Egerton, *Electron Energy-Loss Spectroscopy in the Electron Microscope* (Springer, 2011).
37. O. L. Krivanek, T. C. Lovejoy, N. Dellby, T. Aoki, R. W. Carpenter, P. Rez, E. Soignard, J. Zhu, P. E. Batson, M. J. Lagos, R. F. Egerton, P. A. Crozier, Vibrational spectroscopy in the electron microscope. *Nature* **514**, 209–212 (2014). [doi:10.1038/nature13870](https://doi.org/10.1038/nature13870) [Medline](#)
38. X. Li, G. Haberfehlner, U. Hohenester, O. Stéphan, G. Kothleitner, M. Kociak, Three-dimensional vectorial imaging of surface phonon polaritons. *Science* **371**, 1364–1367 (2021). [doi:10.1126/science.abg0330](https://doi.org/10.1126/science.abg0330) [Medline](#)
39. F. S. Hage, R. J. Nicholls, J. R. Yates, D. G. McCulloch, T. C. Lovejoy, N. Dellby, O. L. Krivanek, K. Refson, Q. M. Ramasse, Nanoscale momentum-resolved vibrational spectroscopy. *Sci. Adv.* **4**, eaar7495 (2018). [doi:10.1126/sciadv.aar7495](https://doi.org/10.1126/sciadv.aar7495) [Medline](#)
40. N. Li, X. Guo, X. Yang, R. Qi, T. Qiao, Y. Li, R. Shi, Y. Li, K. Liu, Z. Xu, L. Liu, F. J. García de Abajo, Q. Dai, E.-G. Wang, P. Gao, Direct observation of highly confined phonon polaritons in suspended monolayer hexagonal boron nitride. *Nat. Mater.* **20**, 43–48 (2021). [doi:10.1038/s41563-020-0763-z](https://doi.org/10.1038/s41563-020-0763-z) [Medline](#)

41. J. Nelayah, M. Kociak, O. Stéphan, F. J. García de Abajo, M. Tencé, L. Henrard, D. Taverna, I. Pastoriza-Santos, L. M. Liz-Marzán, C. Colliex, Mapping surface plasmons on a single metallic nanoparticle. *Nat. Phys.* **3**, 348–353 (2007). [doi:10.1038/nphys575](https://doi.org/10.1038/nphys575)
42. O. Reinhardt, I. Kaminer, Theory of shaping electron wave packets with light. *ACS Photonics* **7**, 2859–2870 (2020). [doi:10.1021/acsp Photonics.0c01133](https://doi.org/10.1021/acsp Photonics.0c01133)
43. M. Mehdi Jadidi, J. S. Ginsberg, G. Patwardhan, S. H. Chae, B. Li, K. Watanabe, T. Taniguchi, J. Hone, A. L. Gaeta, “Phonon-polariton-enhanced nonlinearity in hexagonal boron nitride,” paper FTh4A.6 presented at the 2020 Conference on Lasers and Electro-Optics (CLEO), San Jose, CA, 10 to 15 May 2020.
44. A. A. Popkova, I. M. Antropov, J. E. Fröch, S. Kim, I. Aharonovich, V. O. Bessonov, A. S. Solntsev, A. A. Fedyanin, Optical third-harmonic generation in hexagonal boron nitride thin films. *ACS Photonics* **8**, 824–831 (2021). [doi:10.1021/acsp Photonics.0c01759](https://doi.org/10.1021/acsp Photonics.0c01759)
45. G. M. Vanacore, I. Madan, G. Berruto, K. Wang, E. Pomarico, R. J. Lamb, D. McGrouther, I. Kaminer, B. Barwick, F. J. García de Abajo, F. Carbone, Attosecond coherent control of free-electron wave functions using semi-infinite light fields. *Nat. Commun.* **9**, 2694 (2018). [doi:10.1038/s41467-018-05021-x](https://doi.org/10.1038/s41467-018-05021-x) [Medline](#)
46. A. A. Lanin, A. A. Voronin, A. B. Fedotov, A. M. Zheltikov, Time-domain spectroscopy in the mid-infrared. *Sci. Rep.* **4**, 6670 (2014). [doi:10.1038/srep06670](https://doi.org/10.1038/srep06670) [Medline](#)
47. Y. Wu, J. Ordonez-Miranda, S. Gluchko, R. Anufriev, D. De Sousa Meneses, L. Del Campo, S. Volz, M. Nomura, Enhanced thermal conduction by surface phonon-polaritons. *Sci. Adv.* **6**, eabb4461 (2020). [doi:10.1126/sciadv.abb4461](https://doi.org/10.1126/sciadv.abb4461) [Medline](#)
48. S. Liu, R. He, L. Xue, J. Li, B. Liu, J. H. Edgar, Single crystal growth of millimeter-sized monoisotopic hexagonal boron nitride. *Chem. Mater.* **30**, 6222–6225 (2018). [doi:10.1021/acs.chemmater.8b02589](https://doi.org/10.1021/acs.chemmater.8b02589)
49. T. Malis, S. C. Cheng, R. F. Egerton, EELS log-ratio technique for specimen-thickness measurement in the TEM. *J. Electron Microsc. Tech.* **8**, 193–200 (1988). [doi:10.1002/jemt.1060080206](https://doi.org/10.1002/jemt.1060080206) [Medline](#)
50. H. Shinotsuka, S. Tanuma, C. J. Powell, D. R. Penn, Calculations of electron inelastic mean free paths. XII. Data for 42 inorganic compounds over the 50 eV to 200 keV range with the full Penn algorithm. *Surf. Interface Anal.* **51**, 427–457 (2018). [doi:10.1002/sia.6598](https://doi.org/10.1002/sia.6598) [Medline](#)
51. A. Castellanos-Gomez, M. Buscema, R. Molenaar, V. Singh, L. Janssen, H. S. J. van der Zant, G. A. Steele, Deterministic transfer of two-dimensional materials by all-dry viscoelastic stamping. *2D Mater.* **1**, 011002 (2014). [doi:10.1088/2053-1583/1/1/011002](https://doi.org/10.1088/2053-1583/1/1/011002)
52. R. Frisenda, E. Navarro-Moratalla, P. Gant, D. Pérez De Lara, P. Jarillo-Herrero, R. V. Gorbachev, A. Castellanos-Gomez, Recent progress in the assembly of nanodevices and van der Waals heterostructures by deterministic placement of 2D materials. *Chem. Soc. Rev.* **47**, 53–68 (2018). [doi:10.1039/C7CS00556C](https://doi.org/10.1039/C7CS00556C) [Medline](#)
53. E. J. C. Dias, F. J. García de Abajo, Fundamental limits to the coupling between light and 2D polaritons by small scatterers. *ACS Nano* **13**, 5184–5197 (2019). [doi:10.1021/acsnano.8b09283](https://doi.org/10.1021/acsnano.8b09283) [Medline](#)

54. N. Talebi, *Near-Field-Mediated Photon–Electron Interactions* (Springer, 2019).
55. K. E. Priebe, C. Rathje, S. V. Yalunin, T. Hohage, A. Feist, S. Schäfer, C. Ropers, Attosecond electron pulse trains and quantum state reconstruction in ultrafast transmission electron microscopy. *Nat. Photonics* **11**, 793–797 (2017).  
[doi:10.1038/s41566-017-0045-8](https://doi.org/10.1038/s41566-017-0045-8)
56. M. L. M. Balistreri, H. Gersen, J. P. Korterik, L. Kuipers, N. F. van Hulst, Tracking femtosecond laser pulses in space and time. *Science* **294**, 1080–1082 (2001).  
[doi:10.1126/science.1065163](https://doi.org/10.1126/science.1065163) [Medline](#)
57. Y. Gong, A. G. Joly, D. Hu, P. Z. El-Khoury, W. P. Hess, Ultrafast imaging of surface plasmons propagating on a gold surface. *Nano Lett.* **15**, 3472–3478 (2015).  
[doi:10.1021/acs.nanolett.5b00803](https://doi.org/10.1021/acs.nanolett.5b00803) [Medline](#)
58. G. Spektor, D. Kilbane, A. K. Mahro, B. Frank, S. Ristok, L. Gal, P. Kahl, D. Podbiel, S. Mathias, H. Giessen, F. J. Meyer Zu Heringdorf, M. Orenstein, M. Aeschlimann, Revealing the subfemtosecond dynamics of orbital angular momentum in nanoplasmonic vortices. *Science* **355**, 1187–1191 (2017).  
[doi:10.1126/science.aaj1699](https://doi.org/10.1126/science.aaj1699) [Medline](#)
59. G. Razinskas, D. Kilbane, P. Melchior, P. Geisler, E. Krauss, S. Mathias, B. Hecht, M. Aeschlimann, Normal-incidence PEEM imaging of propagating modes in a plasmonic nanocircuit. *Nano Lett.* **16**, 6832–6837 (2016). [doi:10.1021/acs.nanolett.6b02569](https://doi.org/10.1021/acs.nanolett.6b02569)  
[Medline](#)
60. R. G. Ulbrich, G. W. Fehrenbach, Polariton wave packet propagation in the exciton resonance of a semiconductor. *Phys. Rev. Lett.* **43**, 963–966 (1979).  
[doi:10.1103/PhysRevLett.43.963](https://doi.org/10.1103/PhysRevLett.43.963)
61. K. P. Cheung, D. H. Auston, Excitation of coherent phonon polaritons with femtosecond optical pulses. *Phys. Rev. Lett.* **55**, 2152–2155 (1985).  
[doi:10.1103/PhysRevLett.55.2152](https://doi.org/10.1103/PhysRevLett.55.2152) [Medline](#)